NuSTAR Observations of a Heavily X-Ray-obscured AGN in the Dwarf Galaxy J144013+024744

Shrey Ansh, Chien-Ting J. Chen, W. N. Brandt, Carol E. Hood, E. S. Kammoun, G. Lansbury, Stéphane Paltani, Amy E. Reines, C. Ricci, Douglas A. Swartz, et al.

▶ **To cite this version:**

Shrey Ansh, Chien-Ting J. Chen, W. N. Brandt, Carol E. Hood, E. S. Kammoun, et al.. NuSTAR Observations of a Heavily X-Ray-obscured AGN in the Dwarf Galaxy J144013+024744. The Astrophysical Journal, 2023, 942, ⟨10.3847/1538-4357/ac9382⟩. ⟨insu-04473239⟩

HAL Id: insu-04473239

https://insu.hal.science/insu-04473239v1

Submitted on 22 Feb 2024

HAL is a multi-disciplinary open access archive for the deposit and dissemination of scientific research documents, whether they are published or not. The documents may come from teaching and research institutions in France or abroad, or from public or private research centers.

L'archive ouverte pluridisciplinaire **HAL**, est destinée au dépôt et à la diffusion de documents scientifiques de niveau recherche, publiés ou non, émanant des établissements d'enseignement et de recherche français ou étrangers, des laboratoires publics ou privés.

Distributed under a Creative Commons CC BY 4.0 - Attribution - International License

The Astrophysical Journal, 942:82 (13pp), 2023 January 10 https://doi.org/10.3847/1538-4357/ac9382
© 2023. The Author(s). Published by the American Astronomical Society.
OPEN ACCESS

NuSTAR Observations of a Heavily X-Ray-obscured AGN in the Dwarf Galaxy J144013+024744

Shrey Ansh[1], Chien-Ting J. Chen[2,3], W. N. Brandt[4,5,6], Carol E. Hood[7], E. S. Kammoun[8,9], G. Lansbury[10], Stéphane Paltani[11], Amy E. Reines[12], C. Ricci[13,14], Douglas A. Swartz[2,3], Jonathan R. Trump[15], F. Vito[16], and Ryan C. Hickox[17]

[1] Department of Physics and Astronomy, University of Alabama in Huntsville, 301 Sparkman Dr. NW, Huntsville, AL 35899, USA; sa0124@uah.edu
[2] Science and Technology Institute, Universities Space Research Association, Huntsville, AL 35805, USA; chien-ting.chen@nasa.gov
[3] Astrophysics Office, NASA Marshall Space Flight Center, ST12, Huntsville, AL 35812, USA
[4] Department of Astronomy and Astrophysics, 525 Davey Lab, The Pennsylvania State University, University Park, PA 16802, USA
[5] Institute for Gravitation and the Cosmos, The Pennsylvania State University, University Park, PA 16802, USA
[6] Department of Physics, The Pennsylvania State University, University Park, PA 16802, USA
[7] Department of Physics, California State University, San Bernardino, 5500 University Parkway, San Bernardino, CA 92407, USA
[8] IRAP, Université de Toulouse, CNRS, UPS, CNES 9, Avenue du Colonel Roche, BP 44346, F-31028, Toulouse Cedex 4, France
[9] INAF—Osservatorio Astrofisico di Arcetri, Largo Enrico Fermi 5, I-50125 Firenze, Italy
[10] European Southern Observatory, Karl-Schwarzschild- Strasse 2, D-85748 Garching, Germany
[11] Department of Astronomy, University of Geneva, 1290 Versoix, Switzerland
[12] eXtreme Gravity Institute, Department of Physics, Montana State University, Bozeman, MT 59717, USA
[13] Núcleo de Astronomía de la Facultad de Ingeniería, Universidad Diego Portales, Av. Ejército Libertador 441, Santiago, Chile
[14] Kavli Institute for Astronomy and Astrophysics, Peking University, Beijing 100871, People's Republic of China
[15] Department of Physics, 196A Auditorium Road Unit 3046, University of Connecticut, Storrs, CT 06269 USA
[16] INAF—Osservatorio di Astrofisica e Scienza dello Spazio di Bologna, Via Gobetti 93/3, I-40129 Bologna, Italy
[17] Department of Physics and Astronomy, Dartmouth College, 6127 Wilder Laboratory, Hanover, NH 03755, USA
Received 2022 June 17; revised 2022 September 13; accepted 2022 September 19; published 2023 January 16

Abstract

We present a multiwavelength analysis of the dwarf Seyfert 2 galaxy J144013+024744, a candidate obscured active galactic nucleus (AGN) thought to be powered by an intermediate-mass black hole (IMBH, $M_\bullet \approx 10^4-10^6\ M_\odot$) of mass $M_\bullet \sim 10^{5.2}\ M_\odot$. To study its X-ray properties, we targeted J144013+024744 with NuSTAR for ≈100 ks. The X-ray spectrum was fitted with an absorbed power law, Pexmon, and a physical model (RXTorus). A Bayesian X-ray analysis was performed to estimate the posteriors. The phenomenological and the physical models suggest the AGN to be heavily obscured by a column density of $N_{\rm H} = (3.4\text{–}7.0) \times 10^{23}$ cm^{-2}. In particular, the RXTorus model with a subsolar metallicity suggests the obscuring column to be almost Compton-thick. We compared the 2–10 keV intrinsic X-ray luminosity with the inferred X-ray luminosities based on empirical scaling relations for unobscured AGNs using $L_{[\rm OIV]\ 25.89\ \mu m}$, $L_{[\rm OIII]\ \lambda5007}$, and $L_{6\mu m}$ and found that the high-excitation [OIV] line provides a better estimate of the intrinsic 2–10 keV X-ray luminosity ($L_{2-10}^{\rm int} \sim 10^{41.41}$ erg s^{-1}). Our results suggest that J144013+024744 is the first type 2 dwarf galaxy that shows X-ray spectroscopic evidence for obscuration. The column density that we estimated is among the highest measured to date for IMBH-powered AGNs, implying that a typical AGN torus geometry might extend to the low-mass end. This work has implications for constraining the BH occupation fraction in dwarf galaxies using X-ray observations.

Unified Astronomy Thesaurus concepts: Active galactic nuclei (16)

1. Introduction

There is a general consensus that active galactic nuclei (AGNs) are powered by the accretion of material onto a supermassive black hole (SMBH, $M_\bullet > 10^6\ M_\odot$), but the origin of these SMBHs remains an open question. One of the more quantifiable constraints to differentiate SMBH seeding scenarios is to study the BH occupation fraction in local dwarf galaxies, as they are considered to have undergone fewer mergers and therefore contain the "fossil records" of the first SMBHs (e.g., Volonteri 2010). The first step toward understanding the BH occupation fraction is to understand the full picture of the dwarf galaxy population with an actively accreting nucleus (for a review, see Reines 2022). However, measuring the active fraction is already challenging for these less luminous AGNs that are powered by less massive SMBHs or even intermediate-mass BHs (IMBHs, $M_\bullet \approx 10^4-10^6\ M_\odot$), and obscuration further exacerbates the problem, as typical AGN signatures in soft X-rays and UV–optical bands become almost indiscernible from the stellar emission from their host galaxies (e.g., Grimm et al. 2003; Mineo et al. 2012; Trump et al. 2015).

Reines et al. (2013, hereafter R13) identified 136 optically selected AGNs out of ∼25,000 dwarf emission-line galaxies using Sloan Digital Sky Survey (SDSS) spectroscopy, finding an active fraction of ∼0.5%. Similarly, Baldassare et al. (2018) used ∼28,000 galaxies from SDSS Stripe 82 to search for AGN activity based on optical variability and found that the active fraction decreases with stellar mass and is significantly lower for galaxies with masses $<10^{10}\ M_\odot$. However, measurements from optical surveys are limited, as X-ray and mid-IR surveys have demonstrated that for massive galaxies optical surveys can miss up to 50% of the AGN population (see Hickox & Alexander 2018 for a detailed review). While space-based X-ray and mid-IR observatories have provided a more complete view of the AGN census in massive galaxies, the obscured AGN population in dwarf galaxies remains extremely elusive. This is largely due

Original content from this work may be used under the terms of the Creative Commons Attribution 4.0 licence. Any further distribution of this work must maintain attribution to the author(s) and the title of the work, journal citation and DOI.

to the fact that the luminosity of AGNs in dwarf galaxies can be orders of magnitude lower than that of AGNs in regular galaxies, causing typical AGN identifiers such as optical emission-line ratios and mid-IR colors to be easily buried by the host galaxy light (Trump et al. 2015; Hainline et al. 2016). Moreover, mid-IR searches for AGNs in dwarf galaxies suffer from severe contamination (Satyapal et al. 2014; Kaviraj et al. 2019), as dwarf starburst galaxies can mimic the mid-IR colors of more luminous AGNs (Hainline et al. 2016; Latimer et al. 2021b). On the other hand, X-ray observations are less susceptible to contamination from the host galaxy and are a preferred method to detect AGNs in dwarf galaxies and measure their obscuration level (Xue et al. 2012; Brandt & Alexander 2015; Lemons et al. 2015; Latimer et al. 2021a). In particular, hard X-rays (>10 keV) are extremely useful owing to their strong penetrating power, which can even overcome the heavy obscuration of a torus (Mushotzky 2004).

For AGNs hosted by dwarf galaxies, studies employing X-ray spectral analysis to constrain the properties of the obscuring material remain scarce owing to limited source counts. For the few studies that attempted to do so (Dong et al. 2012; Ludlam et al. 2015; Baldassare et al. 2017), the X-ray spectra of these optically selected broad-line AGNs were largely explained by a simple absorbed power law with little to no obscuration. An exception is NGC 4395. This nearby archetypal IMBH-powered type 1 AGN was found to have highly variable fluxes with evidence for varying partial-covering neutral absorption with a moderate column density of 10^{22}–10^{23} cm^{-2} (Moran et al. 2005; Parker et al. 2015; Kammoun et al. 2019). However, the existence of more heavily obscured (i.e., $N_{\rm H} > 10^{23}$ cm^{-2}) AGNs in local dwarf galaxies remains an open question, although high-redshift X-ray stacking analyses of similar galaxies do suggest that this population exists (e.g., Xue et al. 2012; Mezcua et al. 2016). Therefore, the search for heavily obscured AGNs in dwarf galaxies remains a necessary step for reliably using these systems as a constraint for primordial BH seeding scenarios.

This paper focuses on a promising obscured AGN candidate hosted by the dwarf galaxy J144012.70+024743.5[18,19] (hereafter J1440). J1440 is a dwarf galaxy located at $z = 0.029$ and was selected from the Seyfert 2 low-mass galaxy sample with very low velocity dispersion based on the SDSS data by Barth et al. (2008). Despite its Seyfert 2 classification, R13 identified this target to have a weak broad Hα component in its optical spectrum. The AGN activity can also be confirmed based on Wide-field Infrared Survey Explorer (WISE) selection criteria, which give a magnitude difference between W1 and W2 of 1.14, well above the required difference of 0.77 (Assef et al. 2018). Thornton et al. (2009) used a 22.92 ks exposure with XMM-Newton to study this target (though 25.3% of the exposure time was lost due to background flaring). The signal-to-noise ratio was too low at >1 keV to make any definite conclusion about the column density. Another observation of this target was made in 2015 using Chandra, but the source was not detected in the hard band, and the total counts were too low to perform a spectral analysis (Baldassare et al. 2017). Hood et al. (2017, hereafter H17) followed up the Barth et al. (2008) sample with the Spitzer IRS survey and found some objects in this sample with substantial mid-IR coronal lines such as [NeV] 14.32 μm and [OIV] 25.89 μm. Encouraged by the presence of weak X-ray emission and the high-excitation [OIV] 25.89 μm (see Figure 1) emission line, an AGN marker that is less affected by the host galaxy contamination, we targeted J1440 with the Nuclear Spectroscopic Telescope Array (NuSTAR; Harrison et al. 2013) for 100 ks. Section 2 describes the AGN and galaxy properties of J1440 by fitting the optical–IR photometric data with Code Investigating GALaxy Emission (CIGALE; Boquien et al. 2019). In Section 3, we describe the X-ray spectral models used to fit the NuSTAR data and the results of our X-ray spectral analysis. We supplement our X-ray analysis with multiwavelength data available for J1440 in Section 4. We present our conclusions and discussions in Section 5. In this paper, we used the standard ΛCDM cosmology with $H_o = 70.4$ km s^{-1} Mpc^{-1} and $\Omega_\lambda = 0.73$.

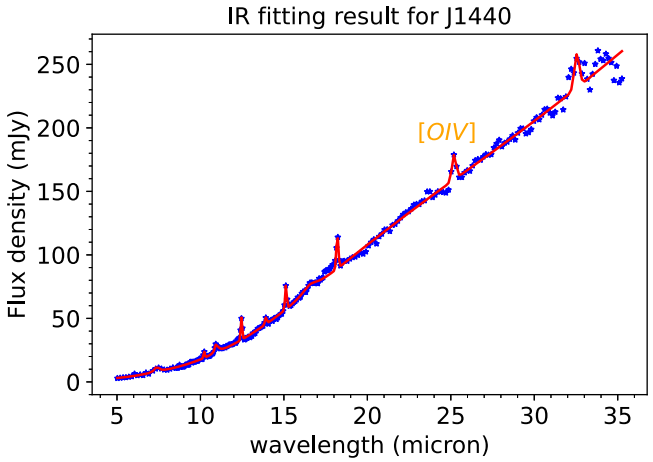

Figure 1. Spitzer IRS spectrum of J1440. The blue stars show the IR spectral data obtained from Spitzer IRS, and the red line shows the model obtained by H17. The presence of the [OIV] 25.89 μm emission line (labeled in the figure) is consistent with AGN activity.

2. Multiwavelength Data for J144013+024744

2.1. Black Hole Mass Estimates

There are multiple ways to estimate the mass of the central BH in galaxies. For instance, bulge-dominated galaxies are expected to trace the $M_\bullet - \sigma_\star$ relation to an acceptable accuracy. Schutte et al. (2019) studied J1440 using deep Hubble Space Telescope (HST)/WFC3 observations and found that J1440 is an Sa galaxy with dim spiral regions in the disk (see Figure 2). J1440 was found to have a classical bulge with a bulge Sérsic index (Sersic 1968) of $n = 1.6$, while the Sérsic index for the disk component was $n = 0.75$. Supported by the presence of a prominent bulge component, we utilize the $M_\bullet - \sigma_\star$ relation derived for low-mass BHs by Xiao et al. (2011): $\log(M_\bullet) = (7.68 \pm 0.08) + (3.32 \pm 0.22)\log(\sigma_\star/200\ {\rm km\,s^{-1}})$. For J1440, this leads to an estimated BH mass of $M_\bullet = 10^{5.5\pm0.2}\ M_\odot$ (based on $\sigma_\star = 44 \pm 4$ km s^{-1} from Barth et al. 2008).

The BH mass can also be estimated from the velocity dispersion of the AGN broad-line region using single-epoch spectra, which is done by assuming the broad-line region gas to be virialized and to follow empirical BH radius–luminosity relations. R13 used the broad Hα line to obtain a viral BH mass estimate of $M_\bullet = 10^{5.2}\ M_\odot$ (see Figure 3 for the fitting of the optical spectrum).

[18] Also known as Tol 1437+030 (Bohuski et al. 1978).
[19] "RCG 32" in R13 sample of dwarf galaxies.

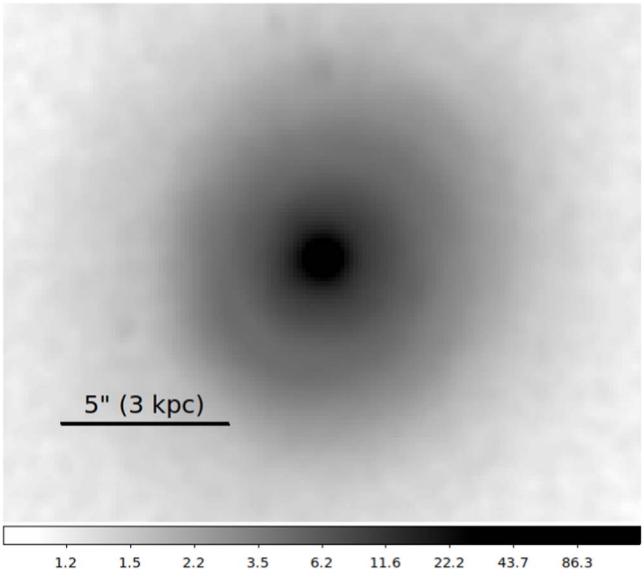

Figure 2. HST WFC3/F110W near-IR image for J1440. The galaxy was classified as a type Sa galaxy in Schutte et al. (2019) with a clear bulge component at its core.

The two $M_{\bullet}$ measurements discussed here are consistent with each other within their respective uncertainties, and both are in the range of what is conventionally considered as an IMBH ($<10^6\ M_{\odot}$).

2.2. SED Fitting Using UV–Optical–IR Photometric Data

In this section, we utilize the existing photometric data of J1440[20] to estimate the physical properties of the galaxy such as its stellar mass, luminosity, star formation rate (SFR), and metallicity using CIGALE. The photometric data we used are as follows: far- and near-UV from GALEX (Kron flux density in an elliptical aperture), optical from SDSS (SDSS model C), near-IR from the Two Micron All Sky Survey (2MASS XSC), and IR from WISE (Profile-fit), Spitzer-MIPS (point-source function flux density), and IRAS (fixed aperture). These photometric data are initially fitted with the modules accounting for the host galaxy emission only. The best-fit spectral energy distribution (SED) deviates from the data significantly at the IR wavelengths, with a poor fit statistic of $\chi^2_{\rm reduced} = 4.06$. This suggests that the galaxy-only modules are not sufficient for J1440. We then include an AGN component, `Fritz2006`, which is an AGN template library composed of an isotropic point-source emission component and a thermal and scattering dust torus emission component (see Fritz et al. 2006; Boquien et al. 2019, for details). This greatly reduced the disagreement between the data and best-fit SED in the IR wavelengths (see Figure 4), with an improved fit statistic of $\chi^2_{\rm reduced} = 1.12$ (for $Z = 0.004$,[21] we discuss the fit statistics for different values of Z later in this section). To confirm the need for an AGN component, we utilized the Akaike information criterion (AIC; Akaike 1974). AIC can be expressed as $\mathrm{AIC} = \chi^2 + 2k$, where χ^2 determines the goodness of fit and was 17.95 for the model including an AGN component and 64.97 for the model with no AGN (galaxy only). AIC penalizes for extra degrees of freedom through k. As we are interested in ΔAIC, the value of Δk on adding the AGN component was 7. A significant result (3σ) is obtained when AIC changes by 7 (see Yang et al. 2018 and references therein). For J1440, $\Delta\mathrm{AIC} = \mathrm{AIC}_{\rm no\ AGN} - \mathrm{AIC}_{\rm AGN}$ was 33.02, which was highly significant and confirmed that an AGN component is required to explain the SED of J1440 (the lower the value of AIC, the better the fit).

For our SED fitting involving both the galactic and AGN components, we explored three different values of metallicity: $Z = 0.0004$, 0.004, and 0.02.[22] The $\chi^2_{\rm reduced}$ for these three metallicities are 0.91, 1.12, and 1.6, respectively. We note that the measurement of metallicities based on photometric SED fits might have limited accuracy, and the spectroscopic measurements can also be challenging owing to the presence of an AGN. However, galaxies with mass similar to J1440 are expected to have lower metallicities than their more massive counterparts, as suggested by the mass–metallicity relation (e.g., Tremonti et al. 2004; Gao et al. 2018). Since the reduced χ^2 for $Z = 0.0004$ and $Z = 0.004$ are both acceptable, we consider the recent study by Ma et al. (2016), who used high-resolution cosmological zoom-in simulations to study the mass–metallicity relation over a wide range of stellar mass and redshift. Using their redshift-dependent mass–metallicity relation and the best-fit $M_{\star}$ for J1440, the expected metallicity for J1440 is $Z = 0.0039$, which is consistent with our choice of metallicity in the CIGALE SED fitting and implies that J1440 is a galaxy with subsolar metallicity. The galactic and AGN properties estimated from the CIGALE SED fitting (for $Z = 0.004$) are as follows:

1. $M_{\star} = 10^{9.20\pm0.05}\ M_{\odot}$ (this stellar mass obtained by CIGALE is slightly lower than that obtained by R13 ($M_{\star} = 10^{9.40}\ M_{\odot}$) using the kcorrect code that fits broadband fluxes using stellar population synthesis models).
2. $\mathrm{SFR} = 0.42 \pm 0.24\ M_{\odot}\,\mathrm{yr}^{-1}$. The SFR and $M_{\star}$ values place J1440 on the star-forming main sequence based on, e.g., Whitaker et al. (2012).
3. $L_{\rm AGN} = (4.33 \pm 0.35) \times 10^{43}$ erg s^{-1} (AGN bolometric luminosity).

We list the input parameter ranges and the best-fit values for all the CIGALE modules in Table 1.

We also compared the SFR obtained from CIGALE with that obtained from the polycyclic aromatic hydrocarbon (PAH) emission (O'Dowd et al. 2009). These complex molecules often break apart when subjected to high-energy photons from the AGN (Schweitzer et al. 2006); therefore, their presence can be used to determine the SFR and the temperature of the dust since these molecules can only form in the colder region of the galaxy (see H17 and references therein). H17 estimated the SFR for J1440 from the PAH features at 7.7 and 11.3 μm. The SFR value of $0.16 \pm 0.10\ M_{\odot}\,\mathrm{yr}^{-1}$ was lower but within the uncertainty range of SFR estimated from CIGALE.

2.3. Existing Soft X-Ray Data from XMM-Newton and Chandra

J1440 was targeted by XMM-Newton in 2006 (XMM-Newton ObsID = 0400570101) with an exposure of 22.92 ks (Thornton et al. 2009), and was also targeted by Chandra in 2015 for ≈6 ks (Chandra ObsID = 17035). The XMM-Newton data were found to be heavily background dominated above 1 keV as suggested by the 4XMM catalog, which is based on the XMM data analysis pipeline provided by the XMMSOC

[20] We collected photometric measurements from the NASA/IPAC Extragalactic Database (NED) (NASA/IPAC 2019).

[21] Here Z is defined as the mass fraction of elements heavier than helium.

[22] With 0.02 being the solar metallicity.

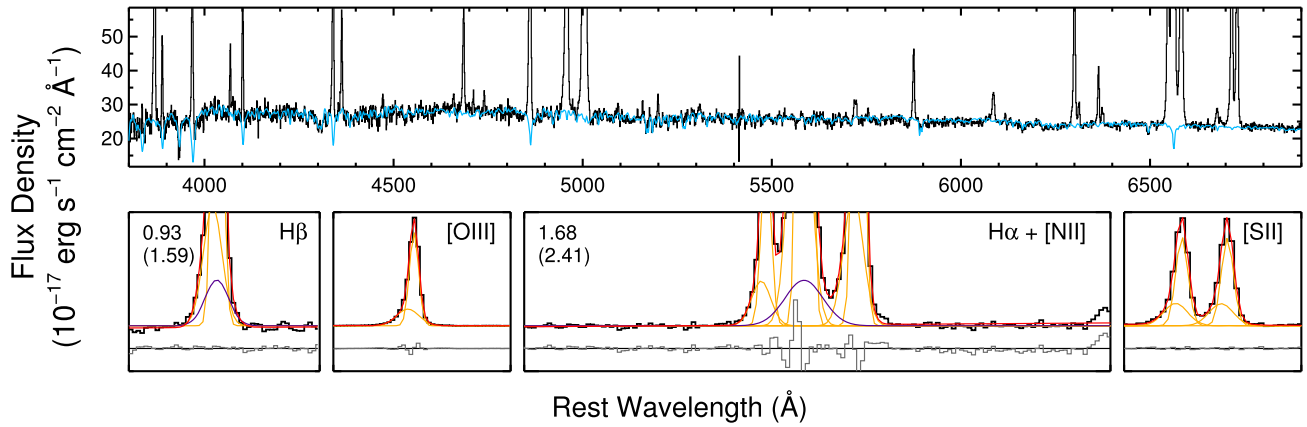

Figure 3. Optical spectrum for J1440 with zoomed-in line profile fits of key emission lines as analyzed in R13. The broad components in Hα and Hβ, as well as the strong [OIII] λ5007 and [SII] lines, are indicative of AGN activities.

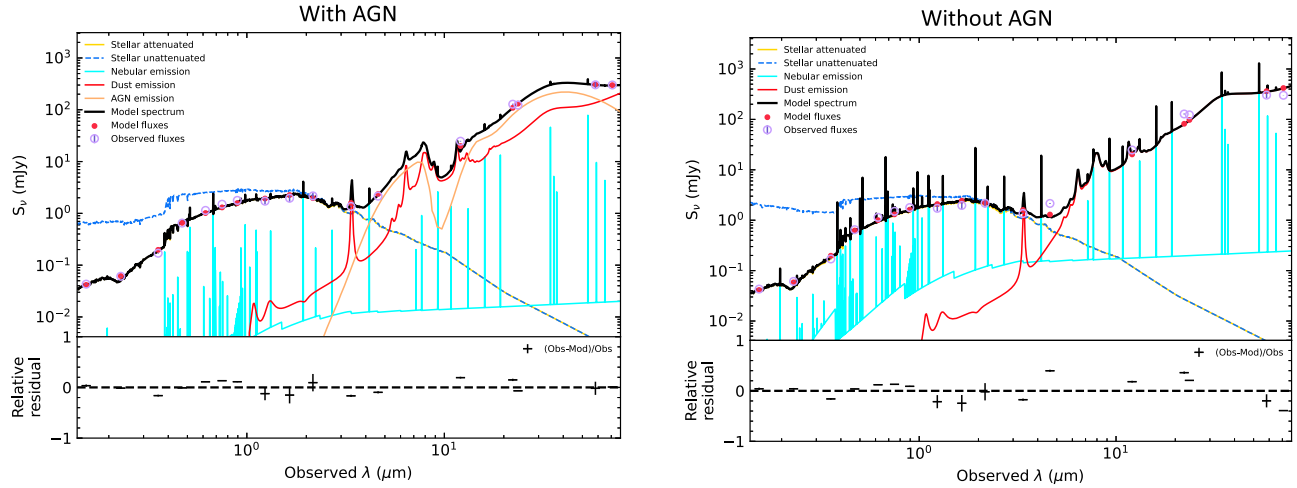

Figure 4. SED fitting of optical–IR photometric data of J1440 using the CIGALE software. The plots with AGN (left) and without AGN (right) are shown with its residual. The higher residual in the right panel suggests the need for an AGN component. Moreover, the AGN component in the optical band is heavily suppressed, which suggests the presence of an obscuring medium.

(Webb et al. 2020). The target was strongly detected in the $<$1 keV bands with DET_ML $>$ 150.[23] However, for harder bands the detection likelihood rapidly drops from $\sim$26 for 1–2 keV to $\sim$8 and $\sim$5 for 2–4.5 keV and 4.5–12 keV bands, respectively. While the source is likely to be detected in the 1–2 keV band according to the 4XMM pipeline software, there are only $\sim 3 \pm 6$ counts in the 1–2 keV band within our spectral extraction region, essentially rendering spectral fitting infeasible beyond 1 keV. Note that the DET_ML values represent the likelihood for the source to be detected according to the algorithm of EMLDETECT, and XMMSOC suggests a minimum of DET_ML = 10 for a reliable detection.[24] Monte Carlo simulations also suggest that the true reliability of a given DET_ML value can be nontrivial. For instance, studies in deep XMM-Newton surveys suggest that the DET_ML values required for a hard (2–12 keV) band source to be detected with a 99.7% (3σ) reliability are $\approx$10 (Chen et al. 2018) or higher (Ni et al. 2021). Due to the background-dominated spectrum for this target, Thornton et al. (2009) were only able to analyze the $<$1 keV spectrum, where they found the object to be dominated by a diffuse plasma model (see Thornton et al. 2009, for details).

The Chandra data were also heavily dominated by the soft X-ray emission with only one $>$2 keV count (see Table 2 in Baldassare et al. 2017), which is effectively a nondetection. Due to the low counts in the Chandra data, no spectral analysis was done in Baldassare et al. (2017). They also found that the soft X-ray flux for this object is consistent with the expected value derived based on the scaling relation between SFR and X-ray luminosity for high-mass X-ray binaries (see their Section 4.1 for details).

Both XMM-Newton and Chandra data suggest that the soft X-ray component for J1440 is not dominated by the X-ray emission from the X-ray corona near the accretion BH, but rather is associated with the host galaxy stellar activity or the diffuse emission in the narrow-line regions (e.g., Bianchi et al. 2006; Bogdán et al. 2017). However, Thornton et al. (2009) suggested that the discrepancy between the soft X-ray emission and the $L_{[\mathrm{OIII}]\ \lambda 5007}$–$L_{2-10\ \mathrm{keV}}$ relation established by Panessa et al. (2006) may imply some level of X-ray obscuration for J1440. This is investigated with NuSTAR observations discussed in the subsequent sections.

[23] DET_ML is the detection maximum likelihood computed by the XMM-Newton source detection, EMLDETECT; see https://xmm-tools.cosmos.esa.int/external/sas/current/doc/emldetect.pdf.

[24] https://www.cosmos.esa.int/web/xmm-newton/sas-thread-src-find-stepbystep

Table 1
CIGALE Templates and Best-Fit Values

Module[a]	Initial Values	Best Fit
(a) sfh2exp		
τ_{main}	100, 300, 1000, 3000, 10000	300
tau_burst	10, 50	10
f_burst	0.01, 0.1	0.1
age	100, 500, 1000, 2000, 5000, 10000	1000
burst_age	10, 25, 50, 100	100
(b) bc03 (Chabrier IMF)		
metallicity	0.004, 0.004, 0.02	
separation_age	10	
(c) nebular		
log U	−3.0	
f_ esc	0.0	
f_ dust	0.0	
lines_width	300.0	
(d) [dustatt_calzleit]		
E_ BVs_young	0.2, 0.4, 0.6, 0.8	0.6
E_BVs_old_factor	0.44	
uv_bump_wavelength	217.5	
uv_bump_width	35.0	
uv_bump_amplitude	1.0, 2.0	2.0
powerlaw_slope	0.0	
(e) dl2007		
qpah	0.47, 1.77, 2.50	1.77
umin	0.10, 0.50, 1.0	1.0
umax	1000000.0	
gamma	0.1	
(f) Fritz2006		
r_ratio	60.0	
tau	3.0, 6.0, 10.0	10.0
beta	−1.00, −0.50, 0.00	−0.50
gamma	0.0	
opening_angle	140	
psy	20.100, 40.100, 60.100	60.100
fracAGN	0.1, 0.3, 0.5	0.5

Note. The modules that we used in the fitting process are as follows: (a) [sfh2exp] models the SFR in terms of decreasing exponential; (b) [bc03] models the intrinsic stellar spectrum; (c) [nebular] calculates the nebular emission lines; (d) [Dustatt_calzleit] models the attenuation due to the dust; (e) [dl2007] calculates reprocessed UV to near-IR emissions due to dust; (f) [fritz2006] models the AGN emission; (g) redshifting.
[a] More details on the individual modules can be found at https://cigale.lam.fr/documentation/.

2.4. NuSTAR Data

The target J1440 was observed on 2020-09-02 for ≈100 ks with NuSTAR, with an obsid 60601028002. The data were processed using HEAsoft v6.29,[25] while NUPIPELINE was used to produce cleaned and calibrated event lists. To account for the background enhancement due to the South Atlantic Anomaly, we set SAA = STRICT and TENTACLE = YES. We selected the source and a source-free background using 45.″00-radius circular regions centered at $(\alpha, \delta) = (14^h40m12^s.66, +02d47m41^s.53)$ and $(14h40m09^s.47, +02d49m49^s.56)$, respectively (Figure 5). NUPRODUCT was used to extract the X-ray spectra of our target from the event files. We generated the spectra for the two Focal Plane Modules (FPM) on board NuSTAR, namely, FPMA and FPMB. The net count rate in the 3–79 keV range for FPMA was $1.56 \times 10^{-3} \pm 4.76 \times 10^{-4}$ counts s^{-1}, while that for FPMB was $1.63 \times 10^{-3} \pm 5.01 \times 10^{-4}$ counts s^{-1}. The cleaned exposure times for FPMA and FPMB were 85.94 and 84.63 ks, respectively.

[25] https://heasarc.gsfc.nasa.gov/docs/software/heasoft/

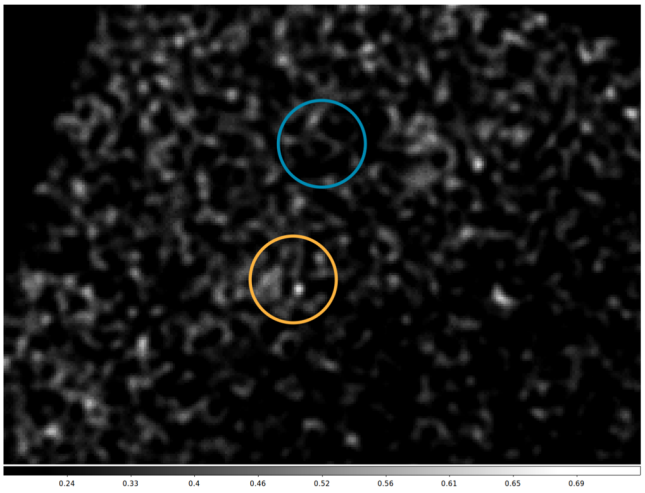

Figure 5. Smoothed 3–24 keV NuSTAR FPMA image of the target J144013 +024744. We define the source and background regions as circles with a 45.″00 radius. The source is represented by a solid orange circle, while the source-free background is represented by a solid blue circle.

To measure the source significance, we followed the algorithm adopted by Mullaney et al. (2015) and Lansbury et al. (2017), which operates on the false-probability images generated based on the NuSTAR background and science images (see Section 2.3 of Mullaney et al. 2015, for further details). The results for the source detection algorithm for the 3–8 keV, 8–24 keV, 3–24 keV, and 30–50 keV bands are summarized in Table 2.

From Table 2, we can infer that the source has significant detections in the 3–8 keV, 8–24 keV, and 3–24 keV bands and is not detected at 30–50 keV. For the 3–24 keV band, where the source is detected most strongly, the source shows a stronger detection in FPMA over FPMB due to lower background.

3. X-Ray Spectral Analyses

In this section, we analyze the NuSTAR spectra of J1440 by fitting them to phenomenological models of different complexity, including a simple absorbed power-law model and the Pexmon model (Nandra et al. 2007) that also takes into account the Compton reflection and fluorescent iron emission lines. We also fit the data with a physical model RXTorus (see Section 3.2 of Paltani & Ricci 2017). The RXTorus model allows for variable metallicity and hence can be useful in modeling the X-ray spectrum of dwarf galaxies, where the metallicity might be significantly lower than for more massive galaxies. This is also motivated by recent studies that suggested that the metal abundance in the AGN torus is comparable to those in the $\sim 10^2 - 10^3$ pc scale narrow-line region (Hikitani et al. 2018). We note that the total X-ray counts for J1440 are limited. The inclusion of physical models in our analysis is to provide some

Table 2
NuSTAR Source Significance for J1440

Band (1)	FPM (2)	Src (3)	Bgd (4)	Bgd_{src} (5)	P_{False} (6)
3–8	A+B	292	712	196.6	1.3×10^{-10}
8–24	A+B	301	847	233.9	9.5×10^{-5}
30–50	A+B	233	820	226.5	0.365
3–24	A+B	592	1553	428.9	5.5×10^{-14}
3–24	A	261	594	164.1	1.9×10^{-12}
3–24	B	331	959	264.9	2.6×10^{-4}

Note. To perform this algorithm, we chose two annuli of sizes 90″ and 160″ for source and background, respectively. Column (1): energy band in keV. Column (2): FPM detectors on which the source detection algorithm was applied, namely FPMA (A) and FPMB (B). Column (3): Src represents the total source + background counts. Column (4): Bgd represents the total background counts in the background region. Column (5): B_{src} represents the background count estimate for the source region. Column (6): P_{False} is the binomial false probability that a signal is coming from random fluctuations rather than the source.

insights into whether the torus models built for typical AGNs can potentially be extended to the lower $M_\bullet$ and $M_\star$ ends, as J1440 is among the few dwarf active galaxies with a nucleus in the IMBH class that are observable with current instruments.

Since the data from FPMB are very heavily background dominated at <7 keV and both the detectors show heavy background domination at >24 keV (see Figure 6), we limit our analysis of NuSTAR data to only the FPMA detector in the 3–24 keV energy range. While there are archival soft X-ray data from Chandra (Baldassare et al. 2017) and XMM-Newton (Thornton et al. 2009), the signal-to-noise ratios for these data are too low at ⩾1 keV to include in our spectral analysis. We use the Bayesian X-ray analysis (BXA; Buchner et al. 2014) software to fit our data. BXA utilizes a nested sampling algorithm[26] to more effectively search for the likelihood maximum when the model parameters exhibit degeneracy. We also utilized BXA's principal component analysis (PCA) based background model for the FPMA detector. The unbinned source spectrum and its background from the FPMA detector were simultaneously fitted (without subtracting) between 3 and 24 keV with different models using the Cash statistic. All these fits were performed with the Sherpa fitting software (Freeman et al. 2001). Regardless of our choice of fitting algorithm and software, the photon index in our fitting could not be constrained owing to the lack of good-quality soft X-ray data; therefore, we fixed the photon index to $\Gamma = 2.13$ (see Section 4.1 for justification of this choice based on multi-wavelength data). In all the models, the metallicity was set to $Z = 0.006$ to account for the likely low metallicity typical for dwarf galaxies (note that the metallicity obtained from the SED fit in Section 2.2 was $Z = 0.004$; however, the minimum Z allowed in RXTorus was 0.006). For our analysis, we ran BXA with 400 live points with the fraction of the integration remainder set at 0.5. Other BXA parameters were set to their default values.

In this work we do not consider a joint analysis of NuSTAR data and the archival XMM-Newton data. This decision is primarily driven by the lack of >1 keV source photons in the XMM-Newton spectra and the fact that the XMM-Newton spectrum was already well fitted with a diffuse hot plasma model (see Section 2.3). Given that the NuSTAR spectrum also has limited counts, a joint analysis that requires both the AGN component and a different soft X-ray component can actually introduce more parameters than the increased degree of freedom, hence making the model parameters even less constrained.

3.1. Phenomenological Models

Before delving into complex physical models, we evaluate the parameters with a simple absorbed power-law model and Pexmon model. The absorbed power-law model in SHERPA can be written as `xstbabs × (xszphabs × xszpowerlw)`. Here `xstbabs` accounts for Galactic absorption and was set to 2.9×10^{20} cm^{-2}.[27] `xszphabs × xszpow` is the redshifted absorbed power law. The best-fit power-law model parameters suggest the source to be heavily obscured with $\log(N_H/\mathrm{cm}^{-2}) = 23.54^{+0.21}_{-0.28}$ (0.16, 0.50, and 0.84 quantiles) and a fit statistic (Cstat/dof) of 507.35/521. The unabsorbed and absorbed 2–10 keV X-ray luminosities for the absorbed power-law model are $\log(L_{2-10}(\mathrm{erg\ s}^{-1})) = 41.41^{+0.12}_{-0.15}$ and $\log(L_{2-10}(\mathrm{erg\ s}^{-1})) = 40.93^{+0.09}_{-0.10}$, respectively (see Figure 7 for spectral fit and residual). If metallicity (Z = 0.006) is included in the absorbed power-law model (using `xsvphabs`), the obscuring column density increases to $\log(N_H/\mathrm{cm}^{-2}) = 24.04^{+0.19}_{-0.28}$.

We also modeled the X-ray spectrum using the Pexmon model, which combines a power law of a fixed cutoff energy with reflection from neutral Compton reflector and fluorescence lines. The model in SHERPA can be written as `xstbabs × (xszphabs × xspexmon)`. We set the inclination angle to 85°, though a different inclination angle did not significantly affect our results. Other parameters of `Pexmon` were set to their default values. The reflection coefficient of `Pexmon` was set to $R = -1$ to simulate a reflection-dominated model, while the cutoff energy was fixed at 400 keV. The column density of $\log(N_H/\mathrm{cm}^{-2}) = 21.47^{+1.16}_{-0.99}$ was poorly constrained, as we were unable to obtain a Gaussian posterior distribution. We then fixed the reflection coefficient to $R = +1$ to include the power-law component. This configuration of Pexmon produced a well-constrained column density (see Figure 8). Since a simple absorbed power law or a Pexmon model does not capture the physics of an obscuring torus, we use physical models to constrain the properties of a physical torus.

3.2. RXTorus

RXTorus is a model of obscuring torus that has a variable ratio of radius of minor to major axis of the torus. The RXTorus model allows for different metallicities of the AGNs (ranging from $Z = 0.006$ to $Z = 0.04$) and hence can be used to model low-metallicity AGNs, particularly those in the dwarf galaxies. Moreover, it also allows for disentanglement of its line-of-sight column density and equatorial column density, which it can measure up to 10^{25} cm^{-2}. The photon index can vary between $\Gamma = 1$ and $\Gamma = 3$. The model in SHERPA can be written as[28] `xstbabs × (RXTorus-cont-0.3 × xscutoffpl`

[26] https://johannesbuchner.github.io/UltraNest/

[27] The value of Galactic column density was calculated using the HEASoft w3nh tool at https://heasarc.gsfc.nasa.gov/cgi-bin/Tools/w3nh/w3nh.pl. We chose the column density obtained from the HI4PI map.

[28] https://www.astro.unige.ch/reflex/

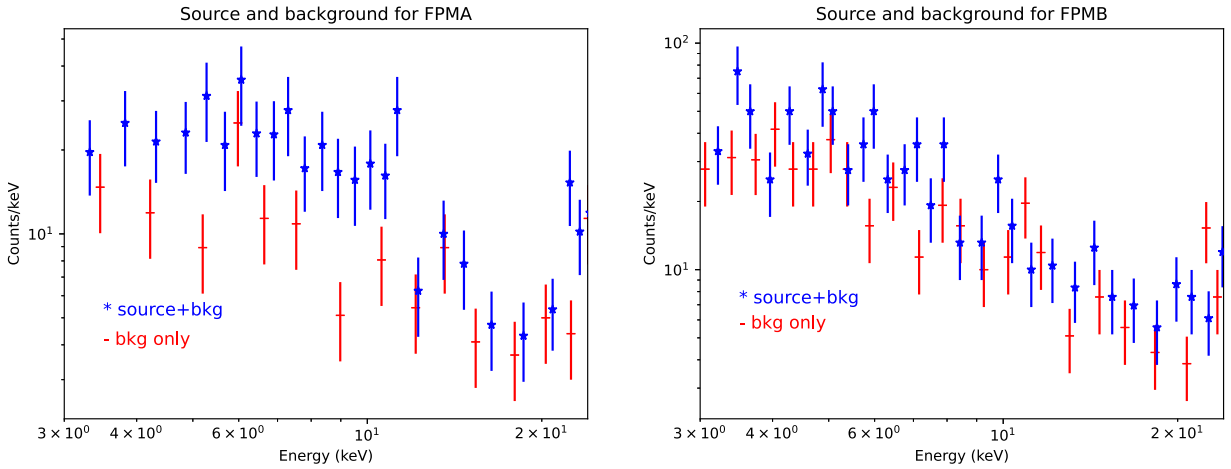

Figure 6. The source and background for the two FPM detectors. Source and background in both the plots are binned at 10 counts bin^{-1} for better display. The FPMB spectrum shows a significantly higher background count at <7 keV than that of FPMA.

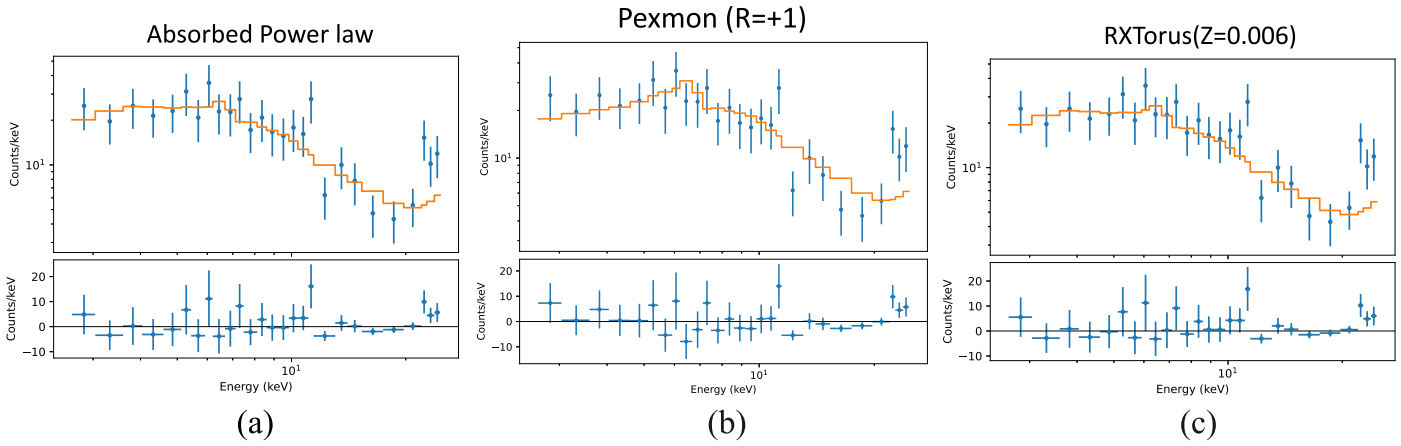

Figure 7. X-ray fitting spectrum for different models: (a) absorbed power-law model; (b) Pexmon model with $R = +1$; and (c) RXTorus model with $Z = 0.006$. The spectrum is binned at 10 counts bin^{-1} for better display.

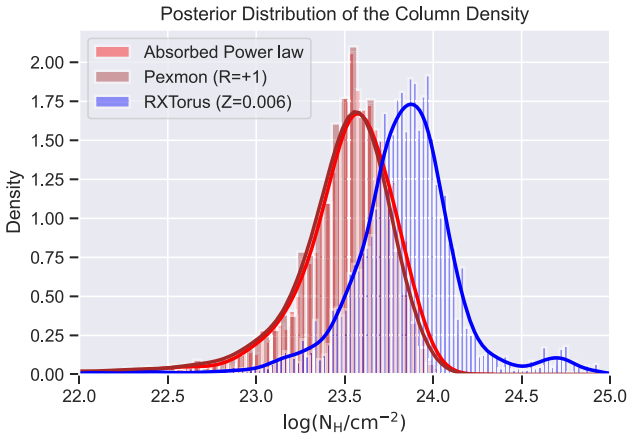

Figure 8. The posterior distribution of the column density for the three models fitted to the NuSTAR data. RXTorus with $Z = 0.006$ produces the highest column density almost in the Compton-thick regime.

+ RXTorus-rprc-0.3). Here RXTorus-cont-0.3 * xscutoffpl is the absorbed power-law component, RXTorus-rprc-0.3 is the reprocessed component that includes scattering and fluorescence emission, and 0.3 represents the metallicity in the unit of solar metallicity of these modules ($Z = 0.006$).[29] In BXA, we created log-uniform priors for RXTorus normalization, column density, and background normalization associated with the FPMA detector, while a uniform prior was created for the inner-to-outer radius ratio of torus (r/R). The photon index, cutoff energy, and column density of all the modules were linked. The cutoff energy was set at 200 keV, the default value of the RXTorus model. The inclination angle was set to 90° to simulate an edge-on viewing; however, we do not find significant changes in the posterior distribution for different inclination angles.

3.3. X-Ray Fitting Results

We show the X-ray fitting results for the phenomenological and physical models in Figure 7. The best-fit parameters of the models discussed in this work are listed in Table 3. We also show the posterior distribution of the best-fit column densities for all the models used in this work in Figure 8. All these models indicate the object to be heavily obscured. For the two phenomenological models simple absorbed power law and Pexmon ($R = +1$), the

[29] The metallicity calculated from CIGALE and the mass–metallicity relation was $Z = 0.004$; however, the lowest metallicity allowed in RXTorus model is $Z = 0.006$.

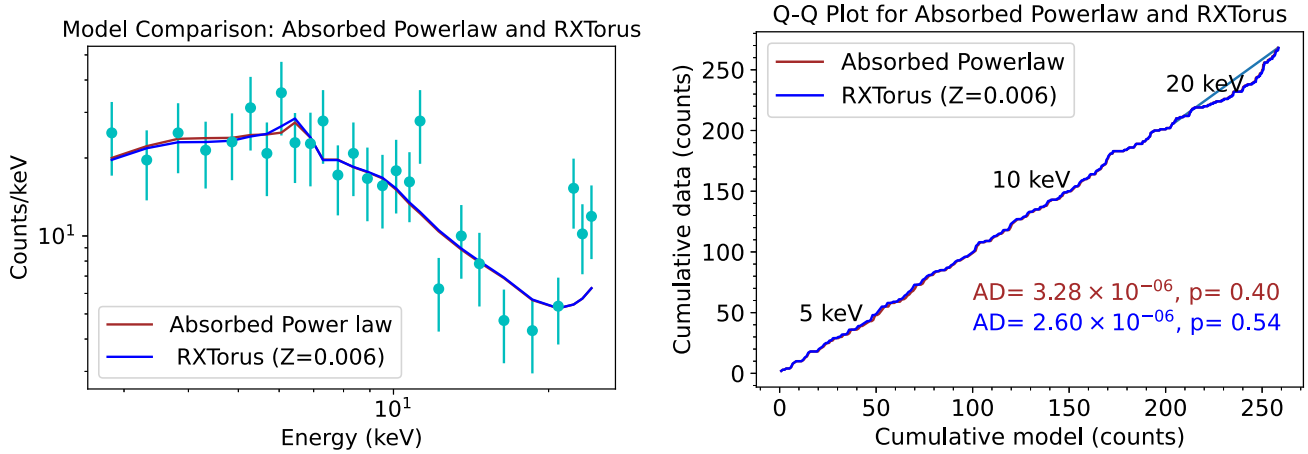

Figure 9. Left: best-fit X-ray spectra for the absorbed power-law model and the physically motivated RXTorus model with $Z = 0.006$. Both these models explained the data reasonably well; however, a mismatch between data and model grows at higher energy (>20 keV). We binned the data to 10 counts bin^{-1} for better display. Right: the cumulative distribution of the unbinned data and the unbinned model plotted in the Quantile–Quantile (Q–Q) plot from 3 to 24 keV. The lower AD-stats and higher p-value for the RXTorus model with $Z = 0.006$ suggest that this physical model might provide a slightly better fit statistics than the absorbed power-law only model. We note that the difference is marginal and a higher-quality spectrum would be required to confirm the presence of a reprocessed component from the putative torus.

Table 3
Posterior Estimates for Different Models

Model	Abs.Powerlw	Pexmon($R = +1$)	RXTorus
$\log\left(\frac{N_{\rm H}}{\rm cm^{-2}}\right)$	$23.54^{+0.21}_{-0.28}$	$23.52^{+0.19}_{-0.29}$	$23.85^{+0.22}_{-0.25}$
$\log(\rm Norm_{zero})$	$-4.15^{+0.12}_{-0.15}$	$-4.22^{+0.12}_{-0.14}$	$-3.98^{+0.25}_{-0.20}$
$\log(\rm Norm_{PCA})$	$2.74^{+0.03}_{-0.03}$	$2.74^{0.03}_{-0.03}$	$2.74^{+0.03}_{-0.03}$
$(\rm CStat/dof)_{source+bkg}$	508.39/521	510.14/526	510.56/521
$(\rm CStat/dof)_{bkgonly}$	393.91/521	393.36/521	393.34/521
$\log(L_{2-10}$ (erg s^{-1}))	$41.41^{+0.12}_{-0.15}$	$41.38^{+0.12}_{-0.14}$	$41.62^{+0.23}_{-0.19}$
$\log(Z)$	-461.65 ± 0.47	-461.12 ± 0.44	-460.26 ± 0.46

Note. The range corresponds to 0.5 quantile with upper bounds corresponding to 0.84 quantile, while lower bound corresponds to 0.16 quantile. Here $\log(\rm Norm_{zero})$ represents the normalization for the zeroth-order power law, and $\log(\rm Norm_{PCA})$ is the normalization for the PCA-based background model associated with FPMA detector.

column densities are $\log(N_{\rm H}/{\rm cm^{-2}}) = 23.54^{+0.21}_{-0.28}$ and $23.52^{+0.19}_{-0.29}$, respectively. For the low-metallicity RXTorus model ($Z = 0.006$), the best-fit column density almost reaches the Compton-thick regime with $\log(N_{\rm H}/{\rm cm^{-2}}) = 23.85^{+0.22}_{-0.25}$). The log-likelihood function that BXA uses to compare models was consistent within margins of error. We do not find significant changes in the column density when a variable inclination angle is used. However, a variable photon index leads to a poor constraint on the column density; hence, it was fixed to $\Gamma = 2.13$. We note that the default cutoff energies are not the same between the physical model and the phenomenological models. However, as demonstrated by Baloković et al. (2020), the intrinsic cutoff energies span a wide range from 140 to 500 keV for 68% of their large sample of AGNs with high-quality NuSTAR and Swift/XRT data. In addition, the spectral fit statistics for their sample do not improve significantly even if the cutoff energy was allowed to vary freely. Therefore, the different cutoff energies are unlikely to qualitatively change our results.

We also show the combined model plot (binned for better display) and the Quantile–Quantile plot (Q–Q plot) of the unbinned data to compare between the absorbed power law and the RXTorus model (Figure 9). All these models explain the data acceptably well, but the models deviate from the data at higher ($\gtrsim$20 keV) energies, possibly due to the high background noise. To quantitatively assess the goodness of the fit, we performed a two-sample Anderson–Darling (AD) test (Anderson & Darling 1954). A two-sample AD test measures the distance between the two cumulative distribution by estimating the square of the difference of the two functions multiplied by a weight function. Since the model was derived from the data, we performed bootstrapping with 2000 iterations to estimate the p-value. These values are quoted in the right panel of Figure 9. The lower AD stat and a higher p-value indicate that the data and model are drawn from the same distribution and corroborate our findings from the Q–Q plot that RXTorus with its subsolar metallicity provides the best fit to the data. In Figure 10 (left) we show the spectral fitting results for the source+background and background-only models. Both the source and background models seem to explain the data reasonably well. The unconvolved model components (Figure 10, right) for the RXTorus models show that the overall spectrum is

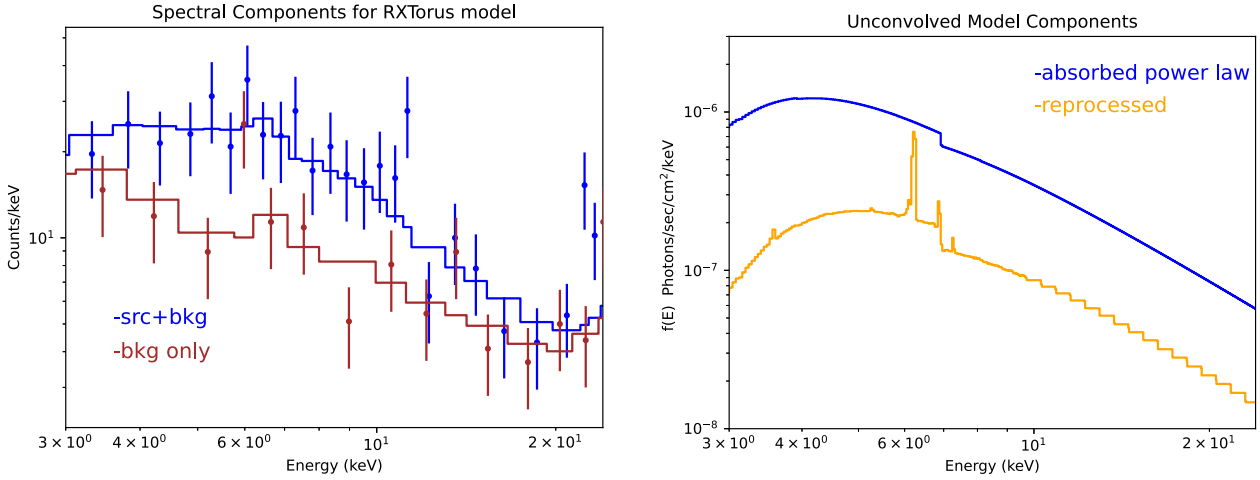

Figure 10. Spectral components. Left: result of simultaneous spectral fitting for the RXTorus model depicting the source + background model and the background model only. Right: to assess the contribution of each of the additive model components, we plotted the unconvolved source spectrum (without the background model) for the RXTorus model. Although the source model is dominated by the absorbed power-law component, we see a nontrivial contribution from the scattered component particularly in the 6.4 keV region. However, the current data prevent us from constraining the width of this Fe line.

dominated by an absorbed power-law component; however, a nonnegligible scattered and fluorescence component is present in the best-fit spectra of physical models. We reiterate that we did not make use of the soft X-ray data from XMM-Newton or Chandra and did not include an additional component to account for the <3 keV emission, due to the lack of high-quality soft X-ray data and the fact that the >3 keV emission for this source cannot be explained with typical diffuse X-ray emission components such as APEC. A high-quality <3 keV X-ray spectrum is needed to further constrain the spectral properties such as the intrinsic photon index and the strength of the scattered and reflected components.

To assess whether the X-ray luminosity of J1440 might have a non-AGN origin, we calculate the expected luminosity from high-mass X-ray binaries (HMXBs) and low-mass X-ray binaries (LMXBs). We used the empirical relation derived by Lehmer et al. (2010), along with the SED-derived SFR and stellar mass discussed in Section 2.2, and find $L_{\rm LMXB} = (1.4 \pm 0.2) \times 10^{38}$ erg s^{-1} and $L_{\rm HMXB} = (6.8 \pm 4)$ erg s^{-1}. We compare this with the 2–10 keV intrinsic luminosity for each model (see Table 3) calculated using SHERPA's "calc_energy_flux" command. This command was applied to the power-law component of the model to obtain the intrinsic luminosity. We find that the intrinsic 2–10 keV X-ray luminosities (Table 3) are $\gtrsim$2 orders of magnitude higher than those expected from X-ray binaries (XRBs). Therefore, the X-ray spectrum of J1440 is unlikely to suffer from significant XRB contamination.

We summarize the key results of our X-ray spectral analysis below:

1. The intrinsic X-ray luminosities for the models discussed in this work are much higher than the expected contribution from X-ray binaries, which strongly supports the presence of a hard X-ray AGN despite the faint soft X-ray fluxes found in the literature (Thornton et al. 2009; Baldassare et al. 2017).
2. All the models indicate the object to be heavily obscured. For the simple absorbed power-law model and Pexmon ($R = +1$) model, the column densities are $\log(N_{\rm H}/{\rm cm}^{-2}) = 23.54^{+0.21}_{-0.28}$ and $23.52^{+0.19}_{-0.29}$, respectively. For the RXTorus model with a low metallicity, the best-fit column density nearly reaches the Compton-thick regime with $\log(N_{\rm H}/{\rm cm}^{-2}) = 23.85^{+0.22}_{-0.25}$.
3. The geometry of the torus was poorly constrained, as we were unable to obtain a Gaussian posterior distribution for the geometry parameter in the RXTorus model. The 0.16, 0.50, and 0.84 quantiles for the ratio of inner to outer radius parameter for the RXTorus model was $0.47^{+0.29}_{-0.25}$. We need more good-quality data to constrain the geometry of the obscuring torus.
4. Qualitatively, the spectra of J1440 are dominated by the absorbed power-law component based on the results from the physical model, but high-quality soft X-ray data and higher signal-to-noise ratio NuSTAR spectra are needed to further constrain the spectral properties.

4. Multiwavelength Properties of J1440

In this section we supplement our findings from the X-ray spectral fitting with the multiwavelength observations of J1440.

4.1. Constraining Photon Index from the Eddington Ratio

As discussed in Section 3, our data quality prohibits us from exploring the full range of the X-ray power-law photon index Γ. We choose the value informed by the multiwavelength data, specifically the AGN bolometric luminosity. For an accreting SMBH, its bolometric luminosity is tied to the global accretion rate, which can affect the seed photon emission and can modulate the X-ray spectral slope (e.g., Shemmer et al. 2006; Ishibashi & Courvoisier 2010). A linear relation between Eddington ratio (λ) and photon index has been documented in the past for systems accreting at high Eddington ratios (e.g., Shemmer et al. 2006, 2008; Brightman et al. 2013; Yang et al. 2015; Trakhtenbrot et al. 2017). In Brightman et al. (2013), the relation can be expressed as $\Gamma = (0.32 \pm 0.05)\log\lambda + (2.27 \pm 0.06)$. For J1440, the bolometric luminosity derived from [OIII] λ5007 is $\log(L_{\rm bol}/{\rm erg\ s}^{-1}) = 43.96 \pm 0.60$ based on the Stern & Laor (2012) empirical relation. Similarly, the bolometric luminosity derived from [OIV] 25.89 μm based on Goulding et al. (2010) is $\log(L_{\rm bol}/{\rm erg\ s}^{-1}) = 42.94 \pm 0.40$. We also calculated the bolometric luminosity directly by integrating the best-fit SED described in Section 2.2 to be $\log(L_{\rm bol}^{\rm SED}/{\rm erg\ s}^{-1}) = 43.64 \pm 0.04$. These values are consistent with each other within the $\sim 1\sigma$ uncertainty. Using the

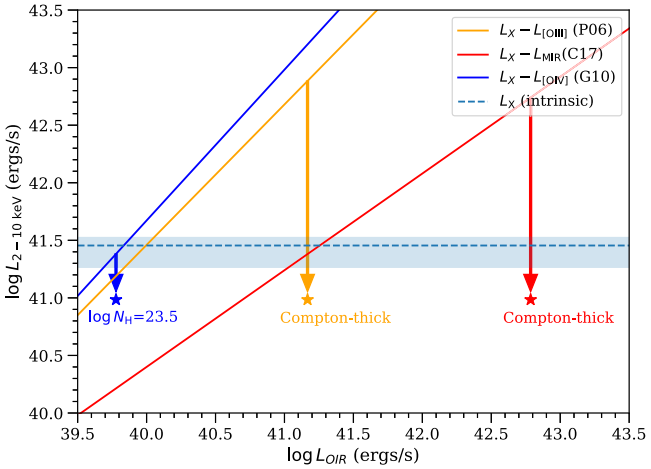

Figure 11. A comparison between the scaling relations between the intrinsic 2–10 keV luminosity and various AGN luminosity indicators derived based on samples of unobscured AGNs, including $L_{2-10\,keV}$ vs. $L_{[OIII]}$ (orange; Panessa et al. 2006, P06), $L_{2-10\,keV}$ vs. $L_{6\mu m}$ (red; Chen et al. 2017, C17), and $L_{2-10\,keV}$ vs. $L_{[OIV]\ 25.89\ \mu m}$ (blue; Goulding et al. 2010, G10). The observed $L_{2-10\,keV}$ and the relevant optical–IR luminosities (L_{OIR}) are shown as the stars. The intrinsic X-ray luminosity (based on a simple absorbed power law with metallicity set at solar metallicity) derived using the NuSTAR observations is shown as the horizontal dashed line, with 1σ uncertainties marked as the shaded region. For large surveys, a common practice is to use the deviation between the observed X-ray luminosity and intrinsic X-ray luminosity based on the scaling relations to estimate the obscuring column density. For J1440, the large deviations between the observed $L_{2-10\,keV}$ and $L_{[OIII]}$ or $L_{6\mu m}$ imply the target to be obscured by Compton-thick materials, while the N_H value inferred from the $L_{2-10\,keV}$ vs. $L_{[OIV]\ 25.89\ \mu m}$ relation is consistent with the X-ray fitting results.

bolometric luminosity from [OIV] 25.89 μm and the BH mass obtained from the broad Hα line, we estimate the Eddington ratio of J1440 to be $\lambda \sim 0.37$. This translates to a photon index of $\Gamma = 2.13 \pm 0.06$ under the assumption of the $\Gamma - \lambda$ relation from Brightman et al. (2013).

A higher photon index for high Eddington ratio, lower-$M_\bullet$ systems has been found in the literature (e.g., Porquet et al. 2004; Done et al. 2012; Baldassare et al. 2017), as low-$M_\bullet$ systems may have a higher accretion disk temperature with thermal emission extending into the soft X-ray energies. Moreover, one can argue that the X-ray photon index could be softer, as J1440 shows the presence of the [OIV] 25.89 μm emission line, which requires an abundance of EUV photons to ionize, and the presence of these EUV photons has been linked to soft X-ray fluxes (Timlin III et al. 2021; Telfer et al. 2002).

4.2. Comparison between Different AGN Luminosity Indicators

While X-ray spectral analysis is an ideal way to confirm the presence of obscuring material in an AGN, the scarcity of sensitive X-ray instruments has limited such observations to only a small number of sources with deep X-ray observations. One commonly adopted practice to find candidate X-ray-obscured AGNs in large surveys is to compare the observed X-ray luminosity and AGN luminosity indicators at other wavelengths, assuming that these different AGN luminosity indicators follow simple scaling relations derived for unobscured type 1 sources. In Figure 11, we compared the 2–10 keV intrinsic luminosity with that from the [OIII] λ5007 (Barth et al. 2008), [OIV] 25.89 μm (H17), and 6 μm (estimated from the SED fits) mid-IR luminosity. The solid orange line represents the L_{2-10} keV versus $L_{[OIII]\ \lambda5007}$ relation obtained by Panessa et al. (2006), where the linear relation can be expressed as $\log\left(\frac{L_{2-10\,keV}}{erg\ s^{-1}}\right) = (1.22 \pm 0.06)\log\left(\frac{L_{[OIII](5007\text{Å})}}{erg\ s^{-1}}\right) + (-7.34 \pm 2.53)$. Similarly, the solid red line shows the L_{2-10} versus $L_{6\mu m}$ relation obtained by Chen et al. (2017). This equation can be expressed as $\log\left(\frac{L_{2-10\,keV}}{erg\ s^{-1}}\right) = (0.84 \pm 0.03) \times \log\left(\frac{L_{6\mu m}}{10^{45} erg\ s^{-1}}\right) + (44.60 \pm 0.01)$. The solid blue line represents the L_{bol} versus $L_{[OIV]\ 25.89\ \mu m}$ relation obtained by Goulding et al. (2010), which can be expressed as $\log\left(\frac{L_{bol}}{10^{44} erg/s}\right) = (0.38 \pm 0.09) + (1.31 \pm 0.09) \times \log\left(\frac{L_{[O[IV]](25.89\mu m)}}{10^{41} erg\ s^{-1}}\right)$. Here we use an X-ray bolometric correction factor of 25 (Brightman et al. 2017) to convert the relation between $L_{2-10\,keV}$ and $L_{[OIV]}$.

With the intrinsic X-ray luminosity and N_H measured for J1440 with NuSTAR, we can assess how effective these different AGN luminosity indicators can be when used to identify heavily obscured AGNs when combined with X-ray observations. For this purpose, we calculated the absorbed 2–10 keV X-ray luminosity by fitting the FPMA data with a simple absorbed power-law model mentioned in Section 3.1, which leads to $\log\left(\frac{L^{abs}_{2-10\,keV}}{erg\ s^{-1}}\right) = 40.93$. If we assumed that the intrinsic AGN X-ray luminosity follows the aforementioned empirical relations, N_H values estimated using the ratio between $L^{abs}_{2-10\,keV}$ and $L_{[OIII]}$ or $L_{6\mu m}$ would be at least an order of magnitude higher than what we obtained from X-ray spectral fitting analysis. On the other hand, the ratio between $L^{abs}_{2-10\,keV}$ and [OIV] 25.89 μm predicts a column density of $\log\left(\frac{N_H}{cm^{-2}}\right) = 23.4$, which is more consistent with the best-fit N_H with phenomenological and physical models described in Section 3. The results are shown in Figure 11. One plausible explanation is that the higher ionization potential of [OIV] (59.4 eV) makes it a better AGN luminosity tracer in dwarf galaxies owing to the more significant host galaxy contamination effects in lines with lower ionization energy such as [OIII] (35 eV) (e.g., Meléndez et al. 2008). As for $L_{6\mu m}$, we see nonnegligible contributions from dust emission associated with stellar activity in the mid-IR wavelength of the best-fit SED. Given the limited photometric coverage in the mid-IR, it is possible that the best-fit AGN SED is still contaminated by the host galaxy contribution. Moreover, if [OIV] 25.89 μm lines are thought to be the better measure of the bolometric luminosity, then CIGALE seems to be overpredicting the bolometric and consequently 6 μm luminosities.

4.3. Optical-to-X-Ray Luminosity Ratio

The ratio between the optical–UV and X-ray luminosity for AGNs has been actively studied in the past, particularly in the parameterized form between the luminosity densities at 2500 Å and 2 keV: $\alpha_{OX} = -0.383\ \log\left(\frac{L_{2500\text{Å}}}{L_{2keV}}\right)$ (Tananbaum et al. 1979). For typical, type 1 AGNs, a clear correlation has been established between α_{OX} and $L_{2500\text{Å}}$ (e.g., Just et al. 2007; Lusso et al. 2010), suggesting that typical AGNs share a common radiation mechanism. However, it is not clear whether this relation extends to AGNs powered by less massive BHs in dwarf galaxies. For instance, the dwarf galaxies in the Baldassare et al. (2017) sample generally deviate from the linear relation, which was primarily attributed to the difficulties in separating AGN emission from that of the host galaxy in such systems (see Section 3.2 of Baldassare et al. 2017). The target studied in this work, J1440, is a part of the

Baldassare et al. (2017) sample and was found to have an α_{OX} lower than the empirical $\alpha_{OX} - L_{2500Å}$ relation for typical AGNs by at least ≈0.6. Here we recalculate α_{OX} for J1440 using the intrinsic 2 keV luminosity based on the best-fit model using NuSTAR data. The UV–optical emission of J1440 is heavily suppressed as shown in Figure 4; therefore, we calculated $L_{2500Å}$ using the power-law relation $f_\nu \propto \nu^{-0.44}$, where we utilized the flux at 5100 Å estimated from the Hα emission line (see Section 4 of Dong et al. 2012 for details of this method).

We find an updated α_{OX} value for J1440 of $\alpha_{OX} = -1.26$. This is consistent with the value expected from the Just et al. (2007) relation within the margin of error. We attribute the different α_{OX} values between our work and that from Baldassare et al. (2017), $\alpha_{OX} = -1.6$, to the presence of AGN obscuration for this object, and the soft X-ray data observed on Chandra and XMM-Newton might have been due to stellar activity of the host galaxy or photoionization of the gas in the AGN narrow-line regions; hence, only the hard X-ray data can give a reliable estimate of intrinsic 2–10 keV X-ray luminosity for heavily obscured AGNs owing to its higher penetrating power. At least for J1440, the IMBH-powered AGN appears to have an optical–UV to X-ray spectral slope similar to typical AGNs. We note that the $L_{2500Å}$ we estimated using empirical relations likely has large uncertainties, but it is consistent with the $L_{2500Å}$ value measured using HST photometry by Baldassare et al. (2017), although the direct photometry measurement is also likely highly uncertain owing to host galaxy contamination. Previous studies of low-mass AGN samples such as Dong et al. (2012) and Baldassare et al. (2017) have found a significant fraction of their sample to deviate away from the empirical $\alpha_{OX} - L_{2500Å}$ relation. The results from J1440 shown here suggest that at least some of the low-mass AGNs still follow the typical α_{OX} relation when obscuration and host galaxy contamination are properly corrected. A NuSTAR follow-up of these low-mass AGNs is thus warranted to study the extension of α_{ox} in low-mass regimes.

4.4. Connecting the IRS Spectrum with the X-Ray Data

Recently Fernández-Ontiveros & Munoz-Darias (2021) studied the IR emission-line ratios for AGNs selected from the Spitzer IRS archive. They found that the ratio between emission lines of different ionizing energies can be used as a proxy of the "hardness" of the ionizing source (i.e., [NeII] 12.81 μm/([NeII] 12.81 μm+[OIV] 25.89 μm); see their Equation (1)). The EUV photons from the accretion disk in rapidly accreting systems can excite high-excitation lines such as [OIV] 25.89 μm from the accretion disk, while the low-excitation lines such as [NeII] 12.81 μm become more significant in systems that lack the strong UV continuum, as they are accreting in a lower state. This transition between different accretion states is commonly seen in XRBs, as their X-ray spectral hardness and count rates cycle through different accretion states (e.g., Fender et al. 2004). However, these transitions are not well studied in the case of AGNs, although some studies suggest that changing-look quasars might be a manifestation of change of state similar to XRBs (Noda & Done 2018). Despite potential uncertainties associated with original sample selection bias, as well as local physical conditions, the mid-IR line ratio provides a useful tool for inferring the "hardness" for AGNs with heavily suppressed and/or soft X-ray emission dominated by host galaxy stellar activity. With the Spitzer IRS emission-line measurements from H17,[30] we can calculate the line ratio defined above to be ≈0.6. Since the Eddington ratio of J1440 is high ($\lambda_{Edd} \approx 0.37$), it could imply that J1440 is currently in the soft accretion state and is transitioning into the hard accretion state. It is possible that [NeII] 12.81 μm has more contamination from the host galaxy for a dwarf galaxy such as J1440. Future spatially resolved observations with JWST's MIRI might help with determining the nuclear line and continuum fluxes, which will reveal more information regarding its accretion mechanisms.

5. Conclusion and Discussion

In this paper we studied J144013+024744, which is an ideal candidate for an obscured AGN in a dwarf galaxy owing to the presence of the high-excitation [OIV] 25.89 μm emission line, an AGN marker that is less affected by host galaxy contamination. We find hard X-ray emission in the NuSTAR data of J1440 consistent with that from an AGN, despite the faint soft X-ray emissions from the archival XMM-Newton ($\log(L_{2-10}/\mathrm{erg\ s^{-1}}) = 40.53 \pm 0.11$) and Chandra data ($\log(L_{2-10}/\mathrm{erg\ s^{-1}}) = 38.79 - 40.36$ (90% confidence)). We fitted the NuSTAR data from the FPMA detector with various physical and phenomenological models and found the object J1440 to be a heavily obscured AGN. The main results are summarized below.

1. The SED fitting with UV–optical–IR photometry confirms that the stellar mass of J1440 ($M_\star = 10^{9.20\pm0.05}\ M_\odot$) is indeed in the dwarf galaxy class, and the fitting result suggests that an AGN component with a bolometric luminosity of $\log(L_{bol}^{SED}/\mathrm{erg\ s^{-1}}) = 43.64 \pm 0.04$ is needed to explain the broadband SED of J1440.
2. The bolometric luminosity estimated from [OIV] 25.89 μm indicates that J1440 is accreting at a relatively high rate, as its bolometric luminosity was close to 37% of its Eddington luminosity. The high Eddington ratio makes spectral analysis possible with NuSTAR observations despite the low BH mass of the AGN in J1440.
3. We fitted the NuSTAR data with phenomenological and physical models. All these models provided a good fit of the NuSTAR data as determined from the quantitative AD test, as well as qualitative tests such as the Quantile–Quantile plots shown in Figure 9. The effect of metallicity might be important for low-metallicity systems such as dwarf galaxies, as we noticed a significant increase in the absorbed column density with the RXTorus model.
4. We compared the intrinsic 2–10 keV X-ray luminosity derived using NuSTAR observations ($L_{2-10}^{int} \sim 10^{41.41}$ erg s^{-1}) with AGN luminosities at other bands, including $L_{[OIII]\ 5007}$, $L_{[OIV]\ 25.89\ \mu m}$, and $L_{6\mu m}$. We find that only $L_{[OIV]\ 25.89\ \mu m}$ traces the intrinsic X-ray luminosity of J1440 in a similar fashion to the empirical $L_{[OIV]\ 25.89\ \mu m} - L_X$ relation for unabsorbed AGNs. This suggests the possibility of searching for more obscured AGNs in dwarf galaxies based on the presence of strong mid-IR fine-structure lines such as [OIV] 25.89 μm. However, a larger sample is required to reliably establish the connection between $L_{[OIV]\ 25.89\ \mu m}$ and hard X-ray luminosities for IMBHs.
5. The optical-to-X-ray flux ratio, α_{OX}, for J1440 agrees with the empirical relation established between α_{OX} and

[30] For J1440 [OIV] 25.89 μm and [NeII] 12.81 μm fluxes are 2.77 ± 0.65 and 3.64 ± 0.70, respectively.

$L_{2500\text{Å}}$ for typical type 1 AGNs. This differs from earlier soft X-ray studies of low-mass AGNs, which typically deviate from this linear relation. However, we do note that measurement of $L_{2500\text{Å}}$ also has significant uncertainty in it. Similar analysis for other IMBH-powered AGNs with NuSTAR can reveal whether this population does follow the extension of the $\alpha_{\rm OX} - L_{2500\text{Å}}$ established for more massive AGNs.

This work provides an important step toward understanding the AGN demographics in dwarf galaxies powered by IMBHs. We showed that heavy X-ray obscuration can occur in AGNs with IMBHs too. It is now widely believed that for more massive galaxies the majority of AGNs are X-ray obscured (Hickox & Alexander 2018). Recently, Tasnim Ananna et al. (2019), using X-ray luminosity functions, showed that the Compton-thick fraction in SMBHs could be as high as ∼50%. If IMBHs in dwarf galaxies are assumed to be just an extension of SMBHs in regular galaxies, then we should expect a similarly high fraction of undiscovered Compton-thick AGNs. J1440 provides a unique opportunity to study the realms of those heavily obscured IMBHs in dwarf galaxies. The fact that even medium-deep soft X-ray observations from Chandra and XMM cannot detect the obscured AGN signal buried in the host galaxy emission highlights the importance of sensitive hard X-ray observations in finding this elusive population. While J1440 is among the highest $\lambda_{\rm Edd}$ dwarf galaxies in the H17 sample, it was still challenging to obtain sufficient hard X-ray counts with a ≈100 ks NuSTAR observation. This highlights the necessity of a next-generation hard X-ray observatory (e.g., HEX-P) for revealing the most elusive AGN population in our cosmic neighborhood. Our results also highlight the potential of mid-IR fine-structure lines for discerning AGN signals in systems with heavy host galaxy contamination. As we enter into the age of JWST, a larger sample size of objects similar to J1440 becomes possible for exploring the physical properties of obscured accreting IMBHs.

We would like to thank the anonymous referee for the helpful comments and suggestions that improved the manuscript. We would also like to thank Johannes Buchner for helping us gain familiarity with the BXA software. This work was supported under NASA grant no. 80NSSC21K0017 and made use of data from the NuSTAR mission, a project led by the California Institute of Technology, managed by the Jet Propulsion Laboratory, and funded by the National Aeronautics and Space Administration. S.A. and C.-T.J.C. also acknowledge support from Chandra X-ray Center AR0-21013A and AR0-21013B. E.S. K. acknowledges financial support from the Centre National d'Etudes Spatiales (CNES).

Software: HEAsoft (NASA High Energy Astrophysics Science Archive Research Center (Heasarc), 2014), Sherpa (Freeman et al. 2001), CIGALE (Boquien et al. 2019), BXA (Buchner et al. 2014).

ORCID iDs

Shrey Ansh https://orcid.org/0000-0002-1016-5488
Chien-Ting J. Chen https://orcid.org/0000-0002-4945-5079
W. N. Brandt https://orcid.org/0000-0002-0167-2453
Carol E. Hood https://orcid.org/0000-0003-0034-5909
E. S. Kammoun https://orcid.org/0000-0002-0273-218X
Stéphane Paltani https://orcid.org/0000-0002-8108-9179
Amy E. Reines https://orcid.org/0000-0001-7158-614X
C. Ricci https://orcid.org/0000-0001-5231-2645
Jonathan R. Trump https://orcid.org/0000-0002-1410-0470
F. Vito https://orcid.org/0000-0003-0680-9305
Ryan C. Hickox https://orcid.org/0000-0003-1468-9526

References

Akaike, H. 1974, ITAC, 19, 716
Anderson, T. W., & Darling, D. A. 1954, J. Am. Stat. Assoc., 49, 765
Assef, R. J., Stern, D., Noirot, G., et al. 2018, ApJS, 234, 23
Baldassare, V. F., Geha, M., & Greene, J. 2018, ApJ, 868, 152
Baldassare, V. F., Reines, A. E., Gallo, E., & Greene, J. E. 2017, ApJ, 836, 20
Baloković, M., Harrison, F. A., Madejski, G., et al. 2020, ApJ, 905, 41
Barth, A. J., Greene, J. E., & Ho, L. C. 2008, AJ, 136, 1179
Bianchi, S., Guainazzi, M., & Chiaberge, M. 2006, A&A, 448, 499
Bogdán, Á., Kraft, R. P., Evans, D. A., Andrade-Santos, F., & Forman, W. R. 2017, ApJ, 848, 61
Bohuski, T. J., Fairall, A. P., & Weedman, D. W. 1978, ApJ, 221, 776
Boquien, M., Burgarella, D., Roehlly, Y., et al. 2019, A&A, 622, A103
Brandt, W. N., & Alexander, D. M. 2015, A&ARv, 23, 1
Brightman, M., Balokovic, M., Baloković, D. R., et al. 2017, ApJ, 844, 10
Brightman, M., Silverman, J. D., Mainieri, V., et al. 2013, MNRAS, 433, 2485
Buchner, J., Georgakakis, A., Nandra, K., et al. 2014, A&A, 564, A125
Chen, C. T. J., Brandt, W. N., Luo, B., et al. 2018, MNRAS, 478, 2132
Chen, C. T. J., Hickox, R. C., Goulding, A. D., et al. 2017, ApJ, 837, 145
Done, C., Davis, S. W., Jin, C., Blaes, O., & Ward, M. 2012, MNRAS, 420, 1848
Dong, R., Greene, J. E., & Ho, L. C. 2012, ApJ, 761, 73
Fender, R. P., Belloni, T. M., & Gallo, E. 2004, MNRAS, 355, 1105
Fernández-Ontiveros, J. A., & Muñoz-Darias, T. 2021, MNRAS, 504, 5726
Freeman, P., Doe, S., & Siemiginowska, A. 2001, Proc. SPIE, 4477, 76
Fritz, J., Franceschini, A., & Hatziminaoglou, E. 2006, MNRAS, 366, 767
Gao, Y., Bao, M., Yuan, Q., et al. 2018, ApJ, 869, 15
Goulding, A. D., Alexander, D. M., Lehmer, B. D., & Mullaney, J. R. 2010, MNRAS, 406, 597
Grimm, H.-J., Gilfanov, M., & Sunyaev, R. 2003, MNRAS, 339, 793
Hainline, K. N., Reines, A. E., Greene, J. E., & Stern, D. 2016, ApJ, 832, 119
Harrison, F. A., Craig, W. W., Christensen, F. E., et al. 2013, ApJ, 770, 103
Hickox, R. C., & Alexander, D. M. 2018, ARA&A, 56, 625
Hikitani, M., Ohno, M., Fukazawa, Y., Kawaguchi, T., & Odaka, H. 2018, ApJ, 867, 80
Hood, C. E., Barth, A. J., Ho, L. C., & Greene, J. E. 2017, ApJ, 838, 26
Ishibashi, W., & Courvoisier, T.-L. 2010, A&A, 512, A58
Just, D. W., Brandt, W. N., Shemmer, O., et al. 2007, ApJ, 665, 1004
Kammoun, E. S., Nardini, E., Zoghbi, A., et al. 2019, ApJ, 886, 145
Kaviraj, S., Martin, G., & Silk, J. 2019, MNRAS, 489, L12
Lansbury, G. B., Stern, D., Aird, J., et al. 2017, ApJ, 836, 99
Latimer, L. J., Reines, A. E., Bogdan, A., & Kraft, R. 2021a, ApJL, 922, L40
Latimer, L. J., Reines, A. E., Hainline, K. N., Greene, J. E., & Stern, D. 2021b, ApJ, 914, 133
Lehmer, B. D., Alexander, D. M., Bauer, F. E., et al. 2010, ApJ, 724, 559
Lemons, S. M., Reines, A. E., Plotkin, R. M., Gallo, E., & Greene, J. E. 2015, ApJ, 805, 12
Ludlam, R. M., Cackett, E. M., Gültekin, K., et al. 2015, MNRAS, 447, 2112
Lusso, E., Comastri, A., Vignali, C., et al. 2010, A&A, 512, A34
Ma, X., Hopkins, P. F., Faucher-Giguère, C.-A., et al. 2016, MNRAS, 456, 2140
Meléndez, M., Kraemer, S. B., Armentrout, B. K., et al. 2008, ApJ, 682, 94
Mezcua, M., Civano, F., Fabbiano, G., Miyaji, T., & Marchesi, S. 2016, ApJ, 817, 20
Mineo, S., Gilfanov, M., & Sunyaev, R. 2012, MNRAS, 419, 2095
Moran, E. C., Eracleous, M., Leighly, K. M., et al. 2005, AJ, 129, 2108
Mullaney, J. R., Del-Moro, A., Aird, J., et al. 2015, ApJ, 808, 184
Mushotzky, R. 2004, Supermassive Black Holes in the Distant Universe (Berlin: Springer), 53
Nandra, K., O'Neill, P. M., George, I. M., & Reeves, J. N. 2007, MNRAS, 382, 194
NASA High Energy Astrophysics Science Archive Research Center (Heasarc) 2014, HEAsoft: Unified Release of FTOOLS and XANADU, Astrophysics Source Code Library, ascl:1408.004
NASA/IPAC Extragalactic Database (NED) 2019, NASA/IPAC Extragalactic Database (NED), IPAC, 10.26132/NED1
Ni, Q., Brandt, W. N., Chen, C.-T., et al. 2021, ApJS, 256, 21
Noda, H., & Done, C. 2018, MNRAS, 480, 3898
O'Dowd, M. J., Schiminovich, D., Johnson, B. D., et al. 2009, ApJ, 705, 885

Paltani, S., & Ricci, C. 2017, A&A, 607, A31
Panessa, F., Bassani, L., Cappi, M., et al. 2006, A&A, 455, 173
Parker, M. L., Fabian, A. C., Matt, G., et al. 2015, MNRAS, 447, 72
Porquet, D., Reeves, J., O'brien, P., & Brinkmann, W. 2004, A&A, 422, 85
Reines, A. E. 2022, NatAs, 6, 26
Reines, A. E., Greene, J. E., & Geha, M. 2013, ApJ, 775, 116
Satyapal, S., Secrest, N. J., McAlpine, W., et al. 2014, ApJ, 784, 113
Schutte, Z., Reines, A. E., & Greene, J. E. 2019, ApJ, 887, 245
Schweitzer, M., Lutz, D., Sturm, E., et al. 2006, ApJ, 649, 79
Sersic, J. L. 1968, (Cordoba, Argentina: Observatorio Astronomico)
Shemmer, O., Brandt, W. N., Netzer, H., Maiolino, R., & Kaspi, S. 2006, ApJL, 646, L29
Shemmer, O., Brandt, W. N., Netzer, H., Maiolino, R., & Kaspi, S. 2008, ApJ, 682, 81
Stern, J., & Laor, A. 2012, MNRAS, 426, 2703
Tananbaum, H., Avni, Y., Branduardi, G., et al. 1979, ApJL, 234, L9
Tasnim Ananna, T., Treister, E., Megan Urry, C., et al. 2019, ApJ, 871, 240
Telfer, R. C., Zheng, W., Kriss, G. A., & Davidsen, A. F. 2002, ApJ, 565, 773
Thornton, C. E., Barth, A. J., Ho, L. C., & Greene, J. E. 2009, ApJ, 705, 1196
Timlin III, J. D., Brandt, W. N., & Laor, A. 2021, MNRAS, 504, 5556
Trakhtenbrot, B., Ricci, C., Koss, M. J., et al. 2017, MNRAS, 470, 800
Tremonti, C. A., Heckman, T. M., Kauffmann, G., et al. 2004, ApJ, 613, 898
Trump, J. R., Sun, M., Zeimann, G. R., et al. 2015, ApJ, 811, 26
Volonteri, M. 2010, A&ARv, 18, 279
Webb, N., Coriat, M., Traulsen, I., et al. 2020, A&A, 641, A136
Whitaker, K. E., van Dokkum, P. G., Brammer, G., & Franx, M. 2012, ApJL, 754, L29
Xiao, T., Barth, A. J., Greene, J. E., et al. 2011, ApJ, 739, 28
Xue, Y. Q., Wang, S. X., Brandt, W. N., et al. 2012, ApJ, 758, 129
Yang, G., Brandt, W. N., Darvish, B., et al. 2018, MNRAS, 480, 1022
Yang, Q.-X., Xie, F.-G., Yuan, F., et al. 2015, MNRAS, 447, 1692